Discover

Research

Investigation of the structural, electrical and magnetic properties of vanadium substituted Mn–Zn ferrites

Atanu Sarker Jyoti[1] · G. G. Biswas[1] · Md. Rasel Rana[1] · Shariful Islam[1] · Md. Emran Hossain[1] · M. N. I. Khan[2] · K. Hoque[1] · Md. Ashraf Ali[3]

© The Author(s) 2023   OPEN

Abstract

This work revealed the role of altering vanadium (V) content in Mn–Zn ferrites. We used the traditional solid-state reaction method to prepare the $Mn_{0.5}Zn_{0.5}V_xFe_{2-x}O_4$ (x = 0.0, 0.05, 0.10, 0.15, 0.20) ferrites. Powder X-ray diffraction was used to analyze the samples' crystal structures, revealing the prepared sample's spinal cubic crystal structure. With increasing Vanadium concentration, the lattice constant drops proportionately. We used Debye–Scherrer (D–S), Williamson–Hall (W–H) Plot, Halder–Wagner (H–W) Langford, and Size Strain Plot (SSP) methods to compare different structural properties. We also used the impedance analyzer to investigate the samples' dielectric characteristics and AC conductivity at room temperature over a frequency range of 1 kHz–100 MHz. The magnetic properties, i.e., Saturation magnetization (Ms), Coercive field (Hc), and Remanent magnetization (Mr), were estimated from the ferromagnetic hysteresis behavior of the samples measured using a vibrating sample magnetometer (VSM). The saturation magnetization was observed to decrease with an increase in V content. The M_r and H_C vary non-linearly with V contents. The prepared samples' initial permeability was tested, and a reasonably constant complex permeability (μ') was recorded over a wide frequency range (~ 1000 Hz).

1 Introduction

Ferrites, crystallized in spinel structures of the cubic system, exhibit exemplary behavior for applications in diverse fields, including the electronic, mechanical-chemical, photocatalytic, magnetic, and biological fields. The applications mentioned above result from their interesting structural, electric, and magnetic properties. The face-centered cubic ferrites consist of two interpenetrating sub-lattices: the tetrahedral (A-sites) and the octahedral (B-sites) sites. The replacement of various ions in the *A* or *B*-sites and their corresponding ratios significantly affect the material's properties [1]. The spin pairing of 3*d* electrons plays a vital role in controlling ferromagnetic oxides' electrical and magnetic properties. The dielectric properties of polycrystalline ferrites are excellent. High dielectric constants in ferrites are advantageous when creating effective microwave devices like switches and isolators [2].

The spinel Mn-Zn ferrite is well known for its excellent initial permeability, minimal power loss, and high saturation magnetization [3]. Since they are soft ferrites, they have a wide range of notable uses as high-frequency

---

✉ K. Hoque, hoquekarimul@phy.ku.ac.bd; ✉ Md. Ashraf Ali, ashrafphy31@cuet.ac.bd | ¹Physics Discipline, Khulna University, Khulna 9208, Bangladesh. ²Atomic Energy Centre, Dhaka 1000, Bangladesh. ³Department of Physics, Chittagong University of Engineering and Technology (CUET), Chattogram 4349, Bangladesh.

magnetic materials, such as the core of inductors and transformers, recording heads, noise filters, rod antennas, switch-mode power suppliesand choke coils [4, 5]. In the area of bio-medicine, Mn-Zn ferrites are also gaining popularity as protein immobilization, magnetic carriers in bio isolation, and other applications [4, 5]. Mn ferrites have antiferromagnetic alignments in their magnetic sub-lattices. They combined spinel structures using the formula $\left(Mn_{0.8}^{2+}Fe_{0.2}^{3+}\right)_A\left[Mn_{0.2}^{2+}Fe_{1.8}^{3+}\right]_B O_4^{2-}$. The full 3$d$ sub-shells of zinc ions make them non-magnetic [4]. They clearly prefer to inhabit the A-sites. So the substitution process occurs at the A-site by substituting Fe^{3+}. As a result, the manganese-zinc ferrite that results has an overall rise in saturation magnetization. Therefore Mn-Zn ferrites are likewise mixed spinels and are typically represented as $\left(Zn_x^{2+}Mn_y^{2+}Fe_{1-x-y}^{3+}\right)_A\left[Mn_{1-x-y}^{2+}Fe_{1+x+y}^{3+}\right]_B O_4^{2-}$[6].

Numerous researchers have discovered that non-magnetic zinc substitution has an impact on the characteristics of Mn ferrites. Somvanshi et al. reported that this spinal ferrites can be used in cancer treatment and many biomedical applications [7–10]. Zinc substitution, by Zapata et al., lowered the Mn-Zn ferrites' Curie temperature [11]. Improvement of electric characteristics by the inclusion of zinc was discovered by Latha et al. [12]. This group asserted that zinc substitutions in manganese ferrites resulted in greater dielectric constants than the parent ferrite. The Mn-Zn ferrites with the following stoichiometry, $Mn_{0.6}Zn_{0.4}Fe_2O_4$, were found to have improved dielectric characteristics and saturation magnetization (M_s) values of 77.30 emu/g by Sun et al. [13]. Our goal was to find a material that would be excellent for the cores of transformers and inductors as well as power applications, among other high-frequency applications, and also had strong magnetic and dielectric properties. As a result, $Mn_{0.5}Zn_{0.5}Fe_2O_4$ was chosen as the parent material. By modifying the type and quantity of defects, a relatively tiny amount of dopant may significantly change the characteristics of Mn-Zn ferrites. The dynamics of grain boundary motion, phase transition temperature, pore clearance, and pore mobility are all impacted by defects [14]. In Mn-Zn ferrites of different stoichiometry, like $Mn_{0.58}Zn_{0.37}Fe_{2.05-x}Gd_xO_4$, $Mn_{0.5}Zn_{0.5}Sc_yFe_{2-y}O_4$, and $Mn_{0.3}Zn_{0.7}Fe_{2-x}Dy_xO_4$, the rare-earth metal substitution results in the 4f–3d coupling, which might enhance magnetic and electrical properties [3, 15, 16].

In the current work, we investigated how the substitution of V in Mn-Zn ferrites affects the electric and magnetic characteristics. Vanadium's effects on cobalt ferrite [17], Ni-Cu–Zn ferrites [18], and lithium zinc titanium ferrite [19, 20] have all been studied. By introducing V^{5+} in Ni–Cu–Zn ferrites, Kaiser et al. observed the development of cation vacancies, which improve pore mobility [21]. As a result, it is anticipated that the vanadium replacement will enhance resistivity, which will in turn cause the leakage current to decrease. Vanadium addition, according to Janghorban and Shokrollahi, improves the magnetic characteristics and grain development of Mn-Zn ferrites up to a point [22]. Most recently Hossain et al. explored that the addition of vanadium shows a decreasing trend of porosity, dielectric constants, and permeability and an increasing trend of grain size, Magnetic saturation (M_s) with an improvement in resistivity [23]. From the aforementioned findings, it can be inferred that vanadium significantly affects the microstructure, which affects the magnetic characteristics. Consequently, we anticipate that the V substitution in the well-known combination $Mn_{0.5}Zn_{0.5}Fe_2O_4$ will contribute to the improvement of its characteristics.

Ferrites' microstructure is also dependent on the sintering process, the caliber of the raw materials, and the material's composition. To attain the desired properties of ferrites, these parameters require to be precisely maintained [4, 24–27]. To obtain a homogeneous and high-density sample, it is essential to choose an appropriate synthesis procedure in light of all of these parameters. Many unconventional methods have produced positive results, yet they have negative effects on the economy and the environment. It is challenging to regulate grain size in the case of the traditional solid-state reaction method. However, by using this method, it can be possible to acquire high-density samples with fewer steps, minimum loss, and affordable costs [28]. As a result, this method is used to create the study samples. The majority of research has concentrated on either the electric or magnetic characteristics of ferrites when vanadium is present. To fully comprehend the material, it is important to simultaneously study its electric and magnetic properties. The main reason to choose this Mn-Zn ferrite matrix is to improve the resistivity. Generally the material used in the transformer core should have high resistivity. Because it reduces the leakage current which produces less heat to the transformer. This inspired us to research both of these V substitution-related issues and contrast our findings with theoretical predictions. In this case, we varied the V concentration to generate a series of $Mn_{0.5}Zn_{0.5}Fe_2O_4$ samples, and we subsequently connected the cation redistribution with the electromagnetic characteristics of Mn-Zn ferrites. In this document, the study's findings are provided.

2 Methods and materials

The ferrites, in powder or thin film forms, can be prepared by hydrothermal technique [29], high-temperature solid-state reaction method [4, 30–33], nitrile-triacetate precursor method [34], solution combustion method [15], sol–gel method [35], co-precipitation method [36, 37], pulsed laser deposition, PVA evaporation method [38], and high-energy ball milling with controlled properties. Due to the simple and cost-effective techniques, a series of ferrites were prepared by solid-state reaction using the traditional two-stage sintering (double-sintering) approach in this study [39]. The parent oxides (low-cost Fe_2O_3), ZnO, MnO, and V_2O_3 are 99.99% pure and were collected from locally available sources.

The stoichiometric quantities of the component compositions were weighted and took exactly 12 gm. The constituent compositions were then blended and hand-milled in an agate mortar for 6 h to bring the particles closer together and ensure homogeneous blending. After that, the powder was heated in a furnace at 700 °C for 3 h and the furnace cooled at the same rate before being mixed using an agate mortar for 2 h. Then the powders were combined with a binder, polyvinyl alcohol, and wet pressed into desired forms with a stainless-steel dies and hydraulic pump. For dielectric, resistivity, and impedance experiments, 0.6 g pellets were made. The 1 g toroids were created to assess permeability. The samples were furnace cooled for 6 h after the second stage sintering at 1150 °C for 4 h in a muffle furnace, resulting in the final product. Figure 1 abbreviates the sample preparation procedures.

To identify the phases synthesized and verify the end of the chemical process and confirm their phase purity, X-ray diffraction (XRD) patterns were obtained using a Phillips PW 3040 X'Pert Pro x-ray diffractometer at BAEC's Atomic Energy Centre (AECD), Dhaka, with $Cu(k_a)$ radiation of an averaged wavelength of 1.54178 Å. The XRD patterns were taken with a step size of 0.02° over an angular range of $2\theta = 20° \sim 70°$ [32, 34]. The X-ray densities and the lattice parameters of the samples from the diffraction pattern were calculated using Eq. (1) [33]. The bulk and mass volume of the samples were used to determine the sintered density. The porosity of each sample was evaluated by comparing the results of both densities.

$$d_x = \frac{8M}{Na^3} \tag{1}$$

where '8' represents the number of molecules in a spinel lattice unit cell, M represents the sample's molecular weight, a is the lattice constant of the ferrite's, and N represents the Avogadro's number. The X-ray density (d_x) is determined by the sample's lattice parameters and molecular weight, whereas the mass density (d) is calculated by the sample's geometry and mass. The following equation was taken to calculate the porosity in percentage (P) of the samples.

Fig. 1 Diagrammatic representation of the sample preparation process for $Mn_{0.5}Zn_{0.5}V_xFe_{2-x}O_4$, for (x=0, x=0.05, x=0.1, x=0.15, x=0.20) via the conventional double sintering technique [31, 40]
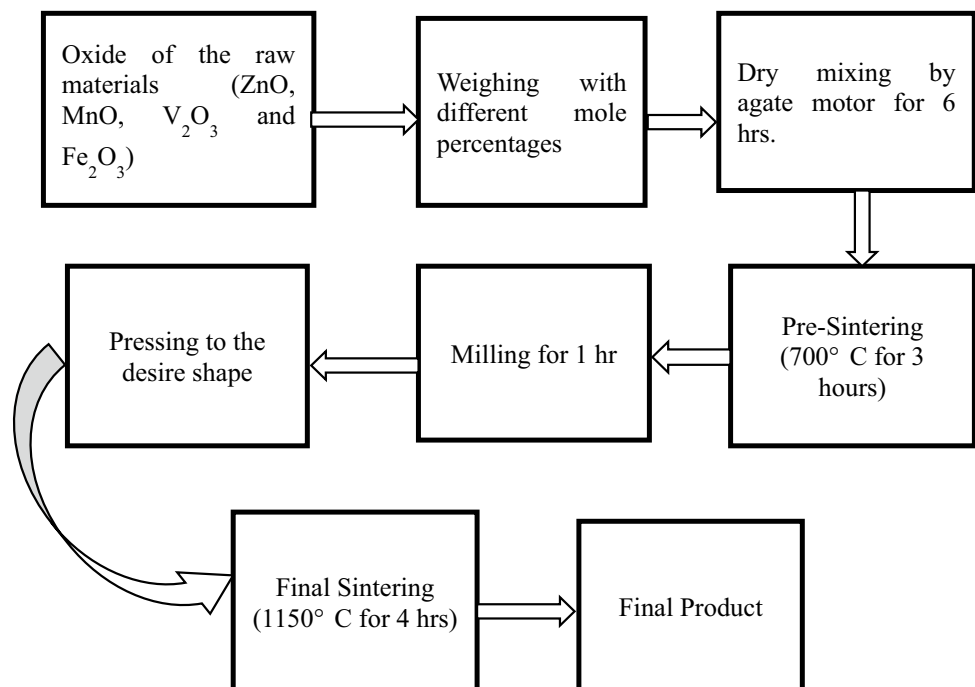
$$P = \frac{1 - \text{bulk density}}{\text{X} - \text{ray density}} \tag{2}$$

3 Different microstructural parameters measurements

3.1 Dislocation density (δ)

The dislocation inside a nanocrystal structure assigns a crystallographic defect or irregularity. As a result, numerous properties of a semiconductor are significantly influenced. The parameters of the unit cell can affect the crystal structure of crystalline solids made up of a periodic array of molecules or atoms. The majority of crystalline solids, however, have dislocations or crystallographic flaws that cause this periodic arrangement of atoms or molecules to break. Other dislocations in the sample prevent some dislocations from migrating. Hence, a large dislocation density implies higher stability. The dislocation density (δ) may be obtained using the relation given below [41], and the outcomes are reported in Table 2.

$$\delta = \frac{1}{D_v{}^2} \tag{3}$$

where D_v is the volume-weighted average crystalline size in nm.

3.2 Stacking fault (SF)

The errors that occur in the sequence of layers of atoms in crystalline materials are known as stacking faults. The energies of stacking faults affect the deformation of metals on a large scale. The stacking fault (SF) may be determined by following equation [29]. Table 2 also shows the SF values for all doping concentrations.

$$SF = \left[\frac{2\pi^2}{45(3 \tan \theta)^{1/2}} \right] \beta \tag{4}$$

3.3 Unit cell volume

The lattice parameters (a = b = c, α = β = γ = 90°, Cubic structure) and also the inter-planar spacing (d) of {h k l} plane were obtained by the following equation,

$$d = \frac{a}{\sqrt{h^2 + k^2 + l^2}} \tag{5}$$

$$2 d \sin \theta = n\lambda \tag{6}$$

The plane is defined by three numbers, h, k, and l, called Miller indices in the preceding formulas, and n represents the order of diffraction (typically n = 1).

The unit cell volume (V) was obtained by the equation below

$$V = a^3 \tag{7}$$

The values of unit cell volume with lattice constant for all doping concentrations are shown in Table 3.

Tables 1 and 2 show the values of several parameters obtained using the D–S approach, W–H, H–W, and SSP methods; they provide almost similar crystallite sizes and lattice strain values. Similar results are also obtained in this study, implying that strain insertion in diverse patterns has little effect on the crystallite size value of Mn-Zn ferrite.

The average crystallite size for pure Mn-Zn ferrite determined using the Debye–Scherrer principle is 11.15 nm. The sizes calculated using the W–H, H–W, and SSP approaches are 7.19 nm, 5.82 nm, and 14.7 nm, respectively. Because the strength of the main peaks (311) grew as the concentration of V doping into the Mn-Zn ferrite lattice increased, the

Table 1 Data for the Strain and the crystallite size obtained by D-S Method, W–H Method, H-W Method, SSP Method of $Mn_{0.5}Zn_{0.5}V_xFe_{2-x}O_4$ ferrites

Sample	Strain $\times 10^{-3}$ (ε)	D-S method	W–H method		H-W method		SSP method	
		D_{D-S}(nm)	D_{WH} (nm)	$\varepsilon_{WH} \times 10^{-3}$	D_{HW} (nm)	$\varepsilon_{HW} \times 10^{-3}$	D_{SSP} (nm)	$\varepsilon_{SSP} \times 10^{-3}$
0.00 M% V	39.1	11.15	7.19	3.5	5.82	7.95	14.7	0.000083
0.05 M% V	26.53	16.34	10.48	2.52	9.43	4.78	14.2	0.00013
0.10 M% V	26.26	15.59	12.36	1.2	12.28	3.11	15.7	0.000084
0.15 M% V	25.41	16.63	11.43	2.03	10.9	4.0	14.7	0.00012
0.20 M% V	29.26	13.93	13.62	0.32	12.63	1.8	16.9	0.000054

Table 2 Data for the Dislocation density obtained by D-S Method, W–H Method, H-W Method, SSP Method and Stacking fault of $Mn_{0.5}Zn_{0.5}V_xFe_{2-x}O_4$ ferrites

Sample	Dislocation density, δ, $\times 10^{14}$ (lines/m^2)				Stacking fault (SF)
	D-S method	W–H method	H-W method	SSP method	
0.00 M% V	102.2	193.4	295	46.5	0.0061
0.05 M% V	44	91	112.4	49.6	0.00412
0.10 M% V	42	65.5	66.3	40.5	0.00411
0.15 M% V	40	76.5	84.2	46.4	0.00395
0.20 M% V	56	53.9	62.7	35.2	0.00463

crystallite size steadily increased, and bigger crystals lowered the overall energy of the system [42]. For 0.05 M% percent V doped concentration, the SSP technique shows a modest reduction in crystallite size.

This decrease in crystallite size might be attributable to an increase in the amount of V atoms, which would apply drag effects on grain development and boundary motion [43]. The rise in V inclusion has been linked to decreased crystalline quality. The incorporation of V atoms may.prevent Mn-Zn ferrite from nucleating, affecting the creation of the host Mn-Zn ferrite structure [44].

The results are compatible with data values for lattice strain (ε) and dislocation density (δ), which are both modified in the opposite direction of crystallite size with V contents (Table 2). The findings estimated using the W–H approach may appear to be more accurate than those calculated using the H-W method because the W–H method fits the data more precisely, where all data points nearly touch the fitting line. It is clear from the ε_{rms} vs ε graphs that the *rms* value linearly changes with ε. And this nature illustrates that the crystallographic orientation of lattice planes is not a source of disagreement [45].

4 Results and discussions

4.1 XRD analysis

All of the ferrite samples were sintered at 1250 °C, and the XRD patterns of the samples are presented in Fig. 2. A very minor peak (222) for x = 0.05 concentration can hardly be seen. So a zoomed picture of this peak is given with the main XRD graph shown in Fig. 2. Compared to the pure samples shown in Fig. 3, the most intense (311) peak migrated toward greater angles as vanadium content increased. According to Bragg's law, the separation between the two crystal surfaces affects the shifting of the diffraction peaks. Strain may be introduced into the lattice by doping ions with varying ionic radii. In Figs. 2 and 3, the tensile strain augmentation induces a peak shift toward lower angles, whereas compressive strain enhancement causes a peak shift toward bigger angles [46]. The impurity level rises as the vanadium content rises since vanadium incorporation causes Fe_2O_3 to precipitate as a second phase [47].

Table 3 shows the cell characteristics of samples sintered at 1250 °C. Vanadium has several valences (3 +, 4 +, 5 +) and may occupy the B-site at lower concentrations in its trivalent form [17], although the characteristics stay generally consistent. The V^{3+} (0.64 Å) and Fe^{3+} (0.645 Å) have nearly identical ionic radii [48]. As a result, no major changes to the cell parameter are anticipated. The decrease in cell parameter is also shown by the displacement of the (311) peak to greater angles. Vanadium increases the densification of samples because of having a melting point of about 670 °C and
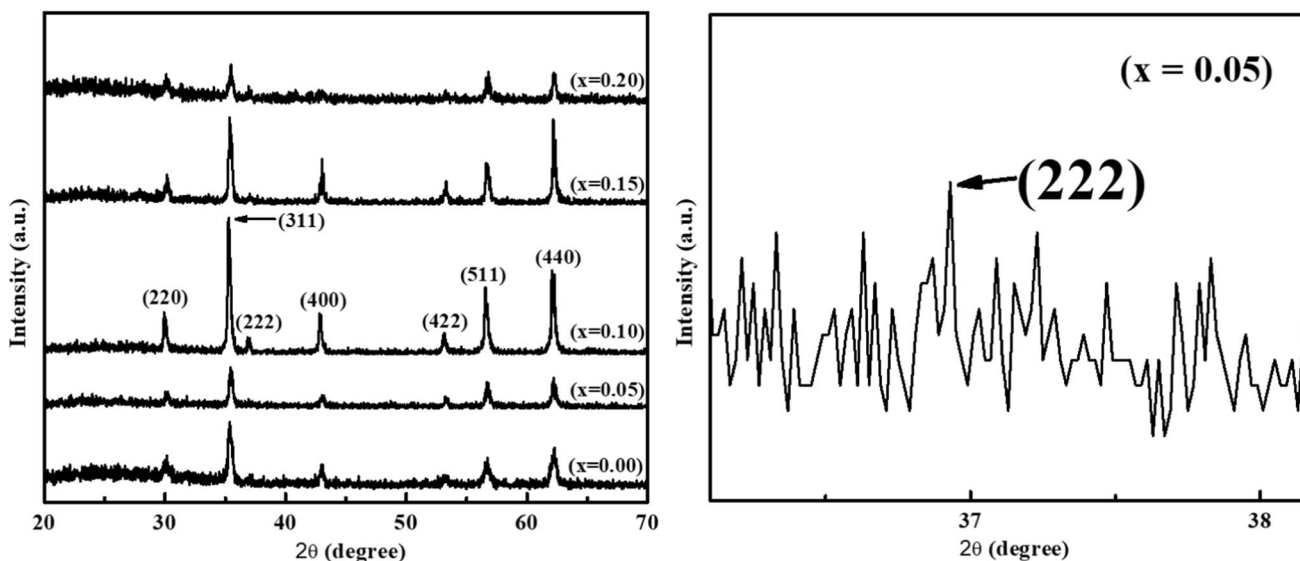
Fig. 2 XRD pattern of Vanadium Substituted $Mn_{0.5}Zn_{0.5}V_xFe_{2-x}O_4$, for (x = 0, x = 0.05, x = 0.1, x = 0.15, x = 0.20)

Fig. 3 XRD patterns (311) of Vanadium Substituted $Mn_{0.5}Zn_{0.5}V_xFe_{2-x}O_4$, for (x = 0, 0.05, 0.1, 0.15, 0.20)
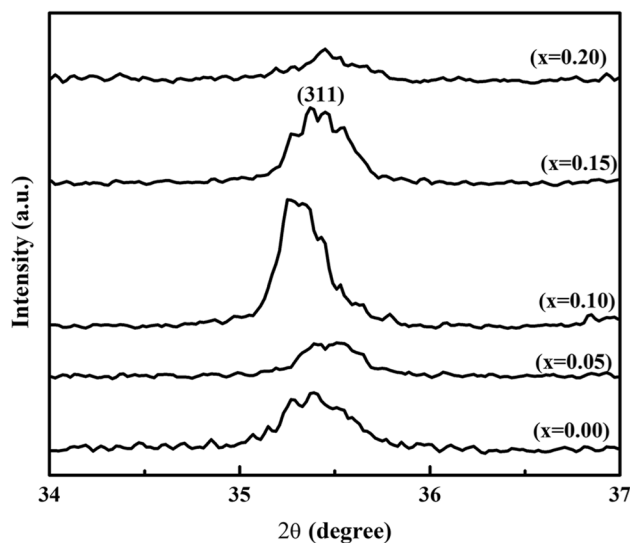

Table 3 The structural parameters of $Mn_{0.5}Zn_{0.5}V_xFe_2xO_4$ ferrites

Composition (x)	Lattice constant $a = b = c$ (Å)	Cell volume a^3(Å^3)	X-ray density, ρ_x	Bulk density, ρ_β	$\phi = \{1-(\rho_\beta/\rho_x)\} \times 100\%$
0.00	8.4169	596.296	5.701	4.20	26.32
0.05	8.4045	593.66	5.789	4.25	26.59
0.10	8.4276	598.558	5.701	4.19	26.47
0.15	8.4106	594.961	5.723	4.101	28.34
0.20	8.4054	593.839	5.777	4.10	29.03

melts at large sintering temperatures [22]. This explains the rising trend in bulk density with vanadium replacement for x = 0.05. The molecular weight and the cell parameter both have an impact on X-ray densities.

With vanadium replacement, these parameters have mostly stayed the same. As a result, there was no discernible difference in X-ray densities. The bulk density has a lower value than the X-ray density because of the porosity formation

during the sintering process [49]. In contrast with bulk density, porosity increases with time, as illustrated in Table 3. It validates the material's Fd-3 m space group membership. As the Vanadium doping concentration is increased, the cell parameters fall. The cell characteristics obtained are also in good accord with earlier Mn–Zn ferrites study [11].

4.2 Debye–Scherrer method

The Scherrer formula was used to compute the crystallite size using the full width at half maximum (FWHM) values generated from the diffraction peaks using the X-ray line broadening technique. In the D-S technique [42], the average crystallite size is defined as the ratio of the root means fourth power to the r.m.s value of the thickness The following is the Debye–Scherrer equation for calculating peak broadening due to an average crystallite size [50]:

$$D = \frac{k\lambda}{\beta_D \cos\theta}$$
(8)

where k represents the form factor, β_D is the value of FWHM, θ represents Bragg's angle, and λ represents the wavelength of X-ray radiation height (FWHM) of the diffraction peak situated at 2θ. The X-ray wavelength (For CuK_α, $\lambda = 1.54056$ Å) and shape factor ($k = 0.94$) are also constants. Table 1 shows the crystallite size values acquired by the Debye–Scherrer technique.

4.3 Williamson–Hall method

Williamson and Hall developed an integral breadth technique for splitting the XRD line broadening caused by lattice strain and crystalline size as a function of a diffraction angle (2θ). The following is the equation's expression:

$$\varepsilon = \frac{1}{4}\beta_s \cot\theta \Rightarrow \beta_s = 4\varepsilon \tan\theta$$
(9)

where micro-strain and integral width owing to strain effect are denoted by ε and β_s, respectively. Cauchy's function [45] is used to quantify the contributions of strain and crystallographic size to line broadening, which are assumed to be independent of one another. The direct sum of β_D and β_s yields the detected line breadth.

$$\beta_{hkl} = \beta_D + \beta_S$$
(10)

Putting the value of β_D from Eq. (10) and the value of β_S from Eq. (9) we have

$$\beta_{hkl} = \frac{k\lambda}{D\cos\theta} + 4\tan\theta$$
(11)

Rearranging

$$\beta_{hkl}\cos\theta = \frac{k\lambda}{D_{WH}} 4\varepsilon_{WH}\sin\theta$$
(12)

The W–H equation in (12) has a straight line and the graph y = $\beta_{hkl}\cos\theta$ against x = 4sinθ is known as the Williamson-Hall (W–H) plot, which is shown in Fig. 4.

The crystalline size was estimated using the y-intercept of the linear fit data, and the slope yielded the strain ε_{WH} value. The strain is expected to be constant for all crystallographic directions, according to Eq. (12) in the W–H technique. With increasing doping concentration, the strain and predicted crystalline size for undoped and doped Mn-Zn ferrites fall and rise, respectively, as shown in Table 1.

4.4 Halder-Wagner method

Another idea made by Halder-Wagner (H-W) must be noted in order to determine D and from XRD data. For the reciprocal cell, an alternate technique was presented that included the integral width, β* is the reciprocal lattice point, and d* the lattice plane spacing as follows [51]:
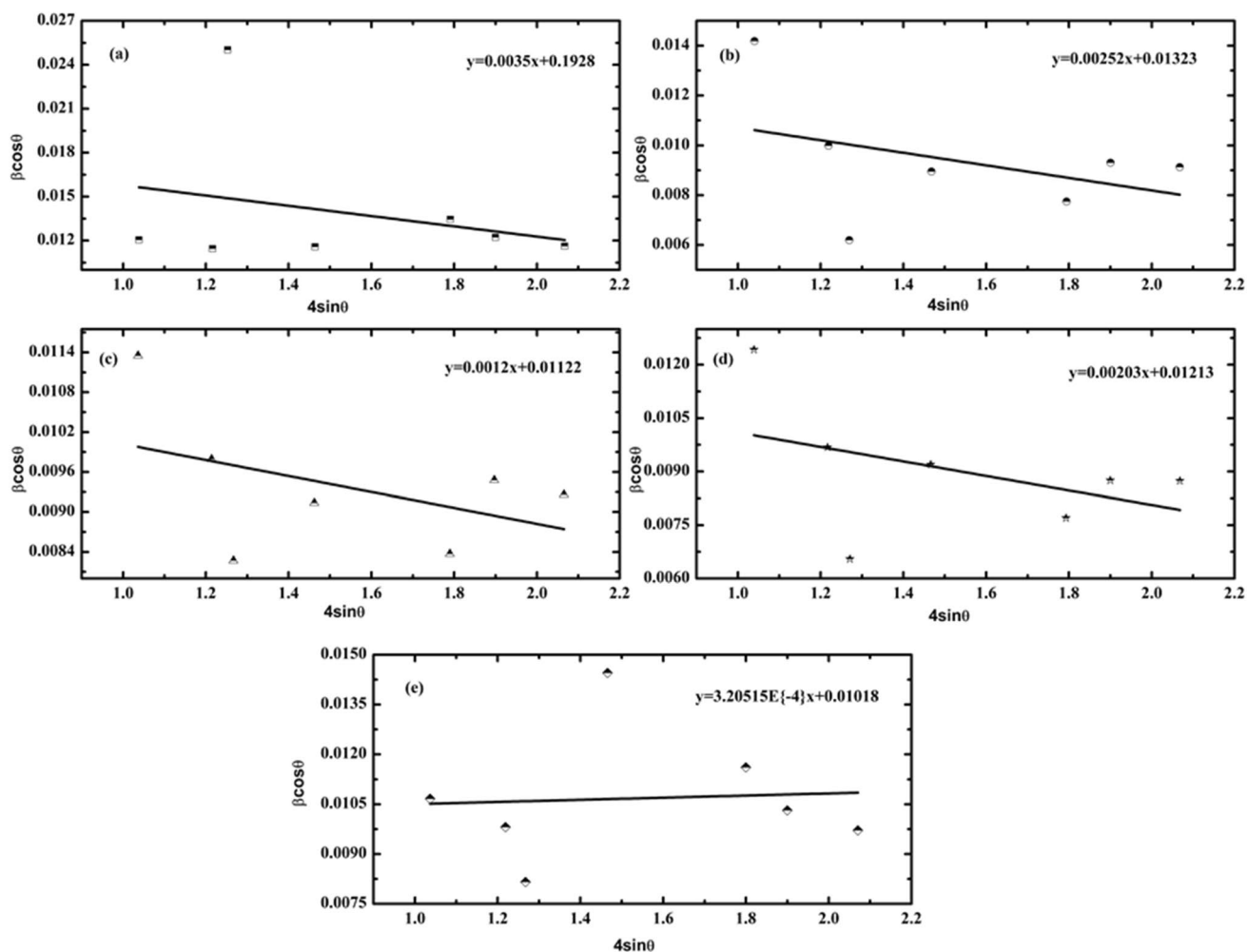
Fig. 4 The W–H plot of Vanadium Substituted $Mn_{0.5}Zn_{0.5}V_xFe_{2-x}O_4$, for (x = 0, x = 0.05, x = 0.1, x = 0.15, x = 0.20)

$$\left(\frac{\beta^*}{d^*}\right)^2 = \frac{k\beta^*}{D_{HW}(d^*)^2} + (2\varepsilon_{HW})^2 \tag{13}$$

where D_{HW} and ε_{HW} are the size and strain of Halder-Wagner crystallites respectively. Then β* and d* are as follows:

$$\beta^* = \frac{\beta cos\theta}{\lambda} \tag{14}$$

$$d^* = \frac{2sin\theta}{\lambda} \tag{15}$$

The Gaussianand Lorentzian components are mostly attributable to strain and size effects, according to this theory. Equation (13) may be expressed using direct space equations as

$$\left(\frac{\beta}{tan\theta}\right)^2 = \frac{K\lambda}{D_{HW}} \cdot \frac{\beta}{tan\theta sin\theta} + 16\varepsilon_{HW}^2 \tag{16}$$

Equation (16) can be rearranged as

$$\left(\frac{\beta cos\theta}{sin\theta}\right)^2 = \frac{K\lambda}{D_{HW}} \cdot \frac{\beta cos\theta}{(sin\theta)^2} + 16\varepsilon_{HW}^2 \qquad (17)$$

The plot of $(\beta/\tan\theta)^2$ against $\beta/(\tan\theta sin\theta)$, yields a straight line with a slope $\frac{K\lambda}{D_{HW}}$ and intercept $16\,\varepsilon_{HW}{}^2$ in the H-W method. As illustrated in Fig. 5, the H-W crystallite size (D_{HW}) and the H-W strain ε_{HW} maybe obtained from the slope and intercept respectively. With increasing doping concentration, the strain and predicted crystalline size for undoped and doped nanorods fall and rise, respectively, as shown in Table 1.

4.5 Size–strain plot (SSP) method

Lattice strain and crystallite size are determined using the SSP approach when it is presumed that the crystal structure is isotropic. A Lorentzian function adjusts the crystallite size in the SSP approximation, whereas a Gaussian function shows the strain [42].

$$(d\beta cos\theta)^2 = \frac{K}{D_{SSP}}\left(d^2\beta cos\theta\right) + \left(\frac{\varepsilon_{SSP}}{2}\right)^2 \qquad (18)$$

Graph of $(d\beta cos\theta)^2$ as the ordinate versus $\left(d^2\beta cos\theta\right)$ as the abscissa is drawn. The estimated data is fitted linearly, and the resultant SSP plots for all XRD peaks are shown in Fig. 6. The D_{SSP} and ε_{SSP} are the slope and the intercept of these plots,
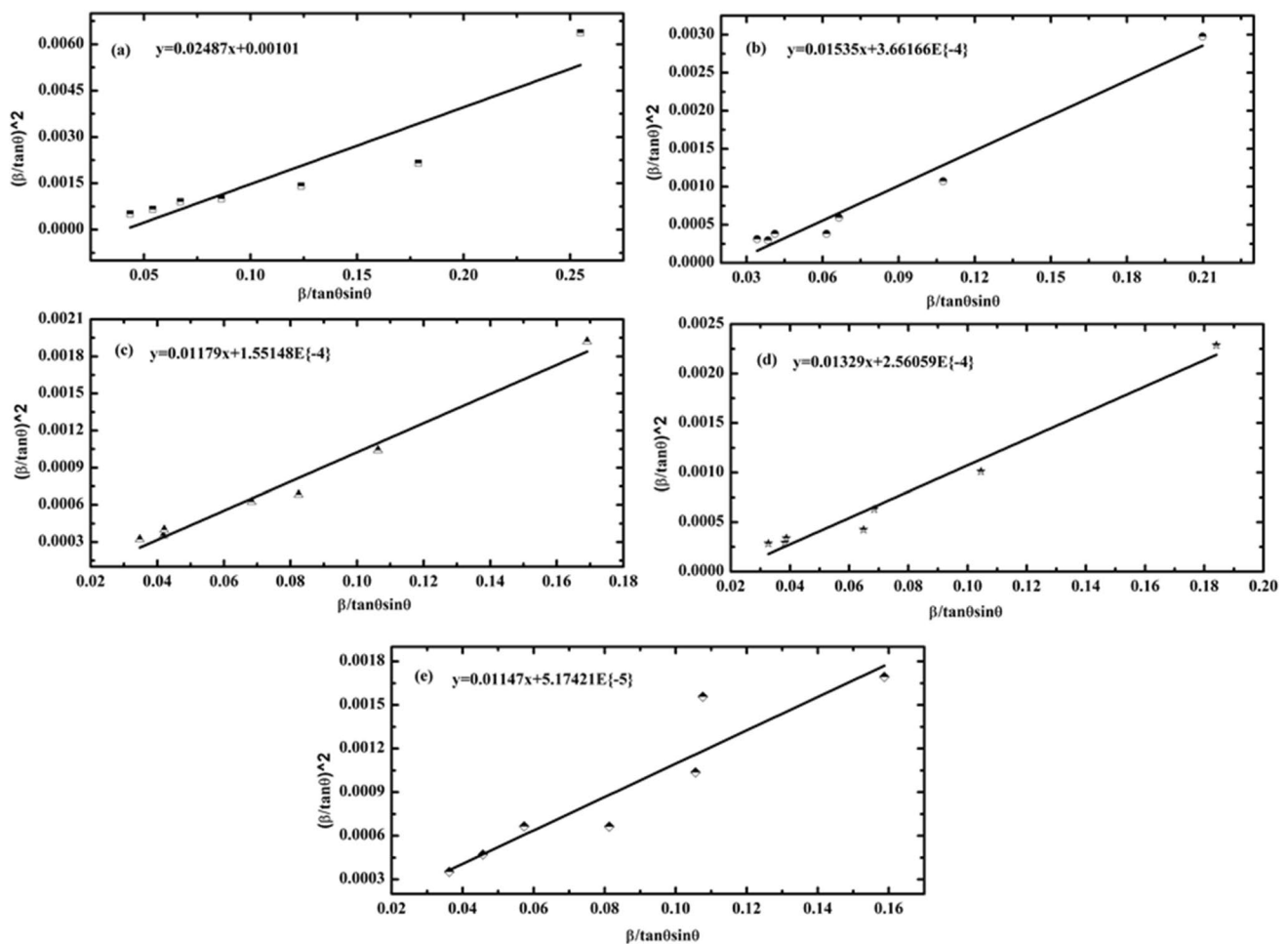
Fig. 5 The H-W plot of Vanadium Substituted $Mn_{0.5}Zn_{0.5}V_xFe_{2-x}O_4$, for (x = 0, x = 0.05, x = 0.1, x = 0.15, x = 0.20)

respectively. With increasing doping concentration, the strain and predicted crystalline size for undoped and doped ferrites rise, as shown in Table 1.

4.6 Lattice strain (ε)

Lattice strain is a measurement of the lattice constant distortion caused by crystal defects i.e., lattice dislocations, stacking faults, flaws, distortions, and so on [34]. The crystal defects are formed due to the displaced atoms regarding lattice positions in crystals. The Stokes-Wilson equation which measures the average lattice strain (ε) in nanorods is given below and the values are charted in Table 1. From Eq. 9, we can write

$$\varepsilon_{hkl} = \frac{\beta_D}{4\tan\theta_{hkl}} \tag{19}$$

4.7 RMS Strain (ε$_{rms}$) estimation

The Stocks-Wilson relationship determines the root mean square micro-strain values (ε_{rms}) along different crystallographic planes.
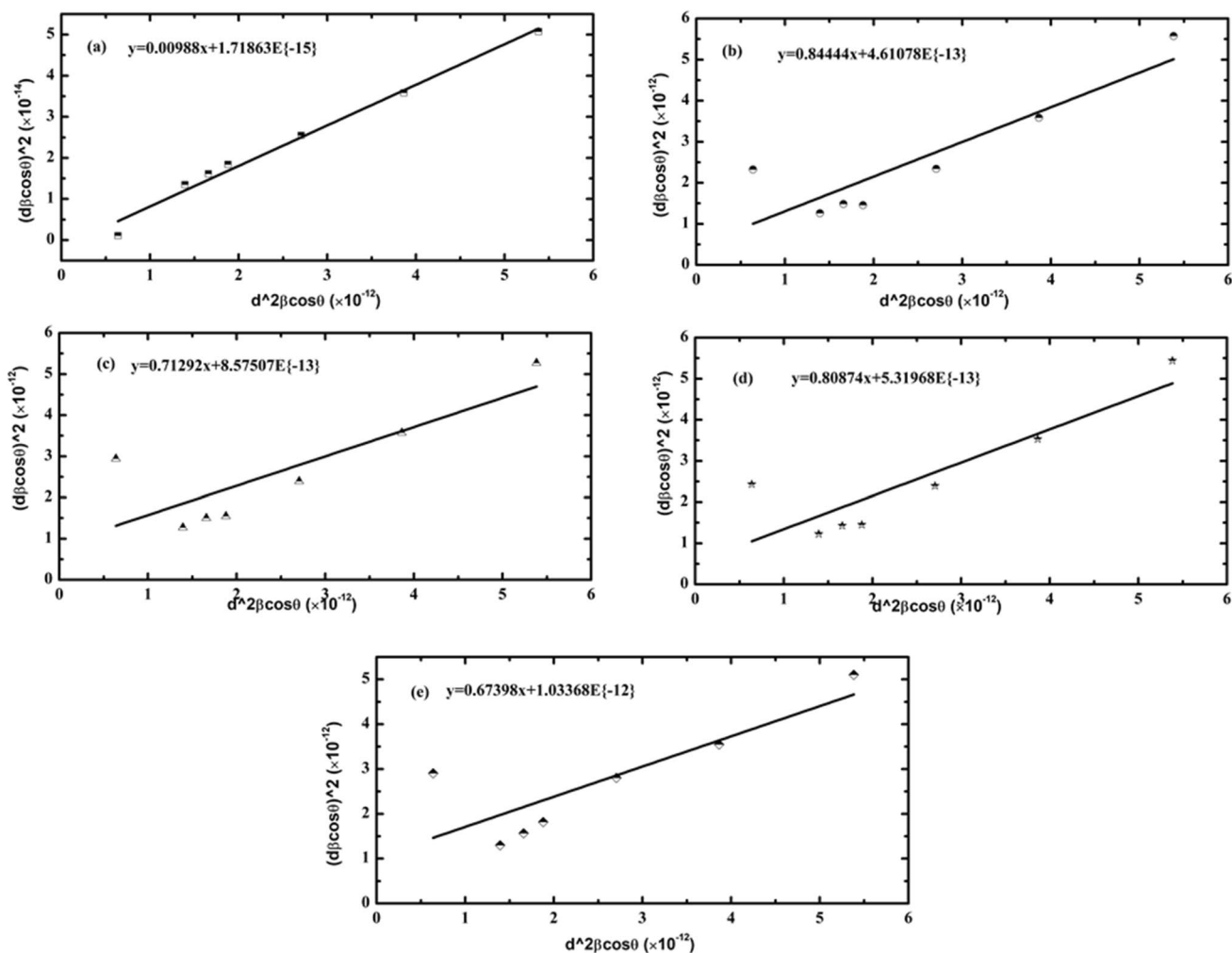
Fig. 6 The SSP plot of Vanadium Substituted Mn$_{0.5}$Zn$_{0.5}$V$_x$Fe$_{2-x}$O$_4$, for (x = 0, x = 0.05, x = 0.1, x = 0.15, x = 0.20)

$$\varepsilon_{rms} = \sqrt{\frac{2}{\pi}}\varepsilon \tag{20}$$

The plot of ε_{rms} against ε is a straight line that makes 45° angle with abscissa and is shown in Fig. 7. There is no disagreement in the crystallographic orientation of lattice planes since the value of root mean square strain varies linearly with micro-strain [30]. The strain may be produced due to a change in lattice characteristics when the doping concentration of V is increased. Various displacement of atoms from their reference lattice positions causes the growth of lattice strain. The diffraction peaks are related to crystalline size as well as to root mean square strain.

4.8 Magnetic properties

Magnetic properties of $Mn_{0.5}Zn_{0.5}V_xFe_{2-x}O_4$ obtained using PPMS is shown in Fig. 8, and several magnetic parameters i.e., saturation magnetization (M_S), coercivity (H_C) and remanent magnetization (M_r) are determined and reported in Table 4. The decrease in M_S is occurs when the V content increases. The decrease in saturation magnetization is due to the reduction in the total magnetic moment of the Ferrites system. The increase of V contents results in the lowering of the Fe^{3+} contents in the B-sites. The magnetic moment of spinel ferrites can be expressed as $M = M_B - M_A$, where M_B and M_A indicates the total magnetic moment at B-sites and A-sites, respectively. Thus, lowering of M_B leads in a decrease in the total moment M, owing to the substitution of Fe^{3+} by V. The variation of M_r and H_C with V contents is nonlinear, which is assumed to be responsible for like magnetic domain walls and associated magnetic moments [52]. The obtained H_C values for the prepared sample are in the range of 129.34–144.62 (Oe), indicating that they are soft magnetic materials [53].
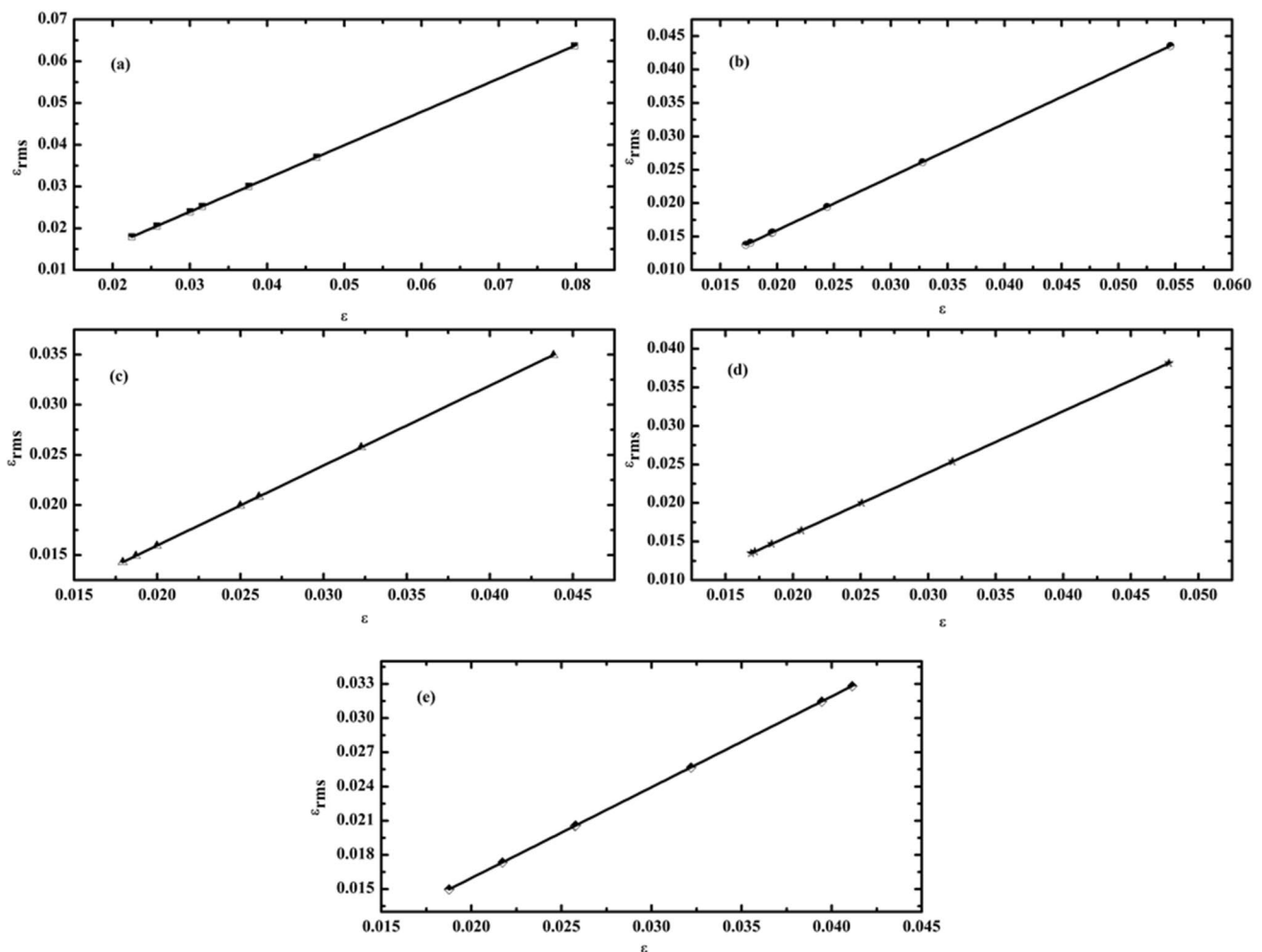

Fig. 7 The ε_{rms} vs ε plot of Vanadium Substituted $Mn_{0.5}Zn_{0.5}V_xFe_{2-x}O_4$, for (x = 0, x = 0.05, x = 0.1, x = 0.15, x = 0.20)

Fig. 8 Plot of Magnetization vs applied magnetic field of Vanadium Substituted $Mn_{0.5}Zn_{0.5}V_xFe_{2-x}O_4$, for (x=0, x=0.05, x=0.1, x=0.15, x=0.20)
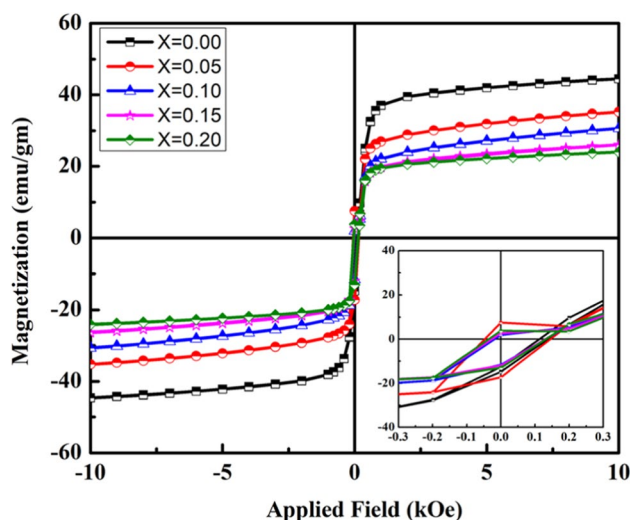

Table 4 Data for magnetic properties of $Mn_{0.5}Zn_{0.5}V_xFe_{2-x}O_4$ ferrites

Sample	Saturation magnetization, M_S (emu/g)	Remanent magnetization, M_r (emu/g)	Coercivity, H_C (Oe)
0.00 M% V	44.512	12.5972	137.7056
0.05 M% V	35.2504	17.2183	144.6194
0.10 M% V	30.63649	12.5964	130.2194
0.15 M% V	26.05097	11.9172	129.3385
0.20 M% V	24.0385	13.015	131.4164

4.9 Permeability

As seen in Fig. 9, the initial permeability μ′ remains constant at lower frequencies before abruptly falling at higher frequencies. The flat region of μ′ is referred to as the utility zone, and it shows how well-synthesized samples are made and how stable they are. In ferrites, permeability is primarily controlled by magnetizing phenomena such as spin rotation and domain wall motion. Over spin rotation, domain wall movement weakens at high frequencies, and then permeability in the high-frequency zone diminishes. In addition, at high frequencies, non-magnetic impurities, grains, and pores function as a catalyst to slow down domain wall motion and spin rotation. With V substitution, the part of complex permeability μ′ is reduced, as seen in Fig. 9. These flaws prevent the domain walls from changing, resulting in a reduction in magnetic characteristics [54]. The sample with x=0.05 & x=0.20 has higher permeability than the un-doped ferrite sample at higher frequencies, indicating more application potential.

As seen in Fig. 10, the imaginary part of permeability μ″ decreases with frequency. This drop with rising frequency denotes a reduction in loss factor at high frequencies, shown in Fig. 11. The lower loss factor indicates that the produced samples have higher high-frequency application potential. Notably, the loss factor occurs when domain wall movement lags behind the field variation. Eddy and residual losses, as well as domain defects, dipole concentration, hysteresis loss, and residual losses, all of them have an impact. The inset displays a close-up of μ″, which is more prominent at high frequencies. This increase is most noticeable near the frequency, in which μ′ drops to about half its initial value.

This effect happens when the frequency of the applied field coincides with the natural frequency of magnetic spins, and the resulting frequency is called a resonance frequency. The Globus model predicts that

$$\sqrt{(\mu_i - 1)}f_r = constant \qquad (21)$$

with f_r being the resonance frequency [55]. As a result, the lower the frequency where resonance occurs, the higher the permeability, and vice versa. This notion is in line with the final product. The decrease in permeability causes the resonance peak to move to a higher frequency as V increases. This also restricts the frequency range in which the processed samples may be used. Figure 12 shows how the quality factor (Q) varies with respect to the frequency. It has been shown

Fig. 9 The frequency dependence of μ´of Vanadium Substituted $Mn_{0.5}Zn_{0.5}V_xFe_{2-x}O_4$, for (x=0, x=0.05, x=0.1, x=0.15, x=0.20)
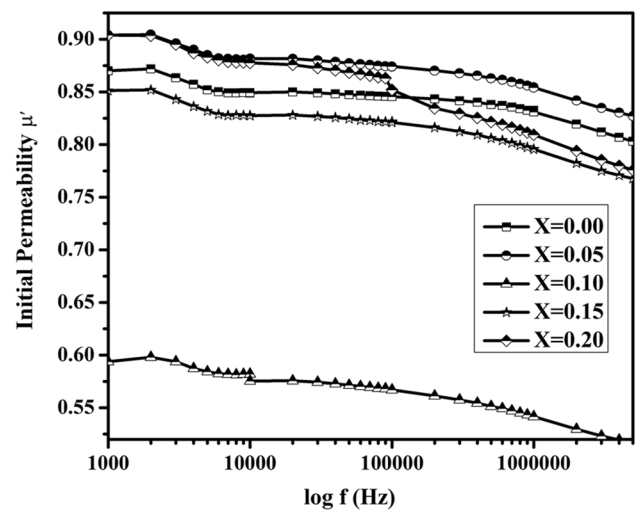

Fig. 10 The frequency dependence of μ″of Vanadium Substituted $Mn_{0.5}Zn_{0.5}V_xFe_{2-x}O_4$, for (x=0, x=0.05, x=0.1, x=0.15, x=0.20)
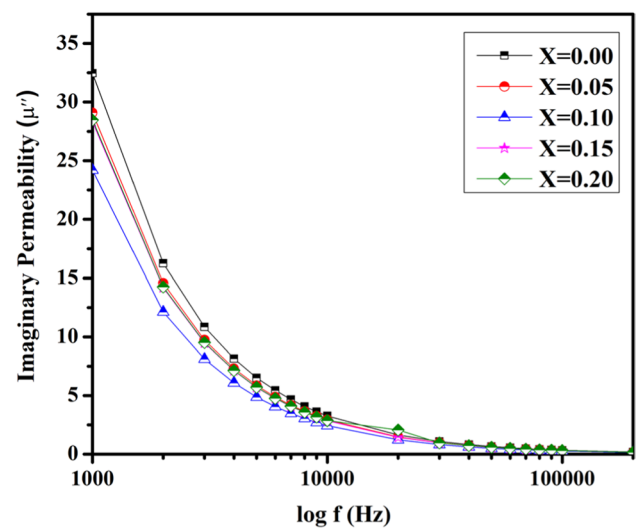

Fig. 11 The frequency dependence of magnetic loss tangent (tanδ) of Vanadium Substituted $Mn_{0.5}Zn_{0.5}V_xFe_{2-x}O_4$, for (x=0, x=0.05, x=0.1, x=0.15, x=0.20)
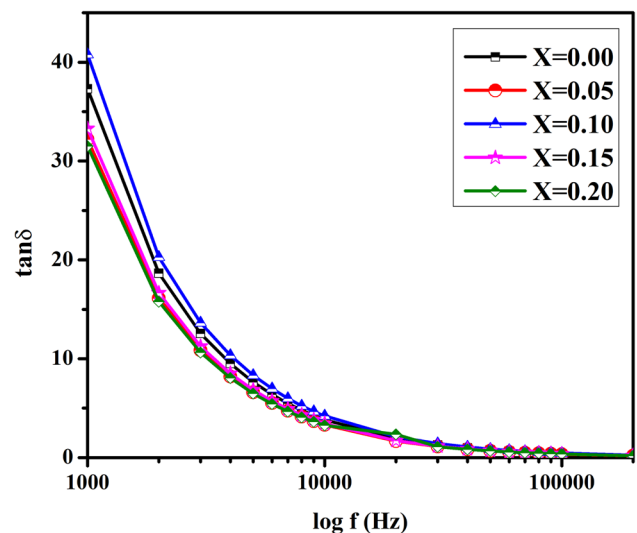
Fig. 12 The frequency dependence of Q-factor of Vanadium Substituted $Mn_{0.5}Zn_{0.5}V_xFe_{2-x}O_4$, for (x=0, x=0.05, x=0.1, x=0.15, x=0.20)
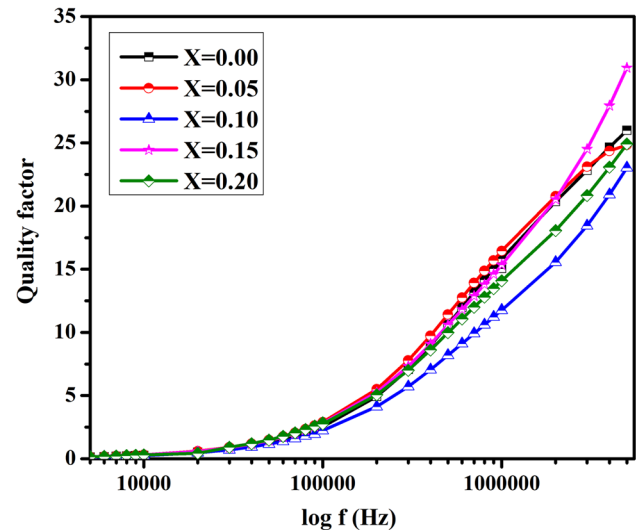
Fig. 13 The frequency dependence of ε´ of Vanadium Substituted $Mn_{0.5}Zn_{0.5}V_xFe_{2-x}O_4$, for (x=0, x=0.05, x=0.1, x=0.15, x=0.20)
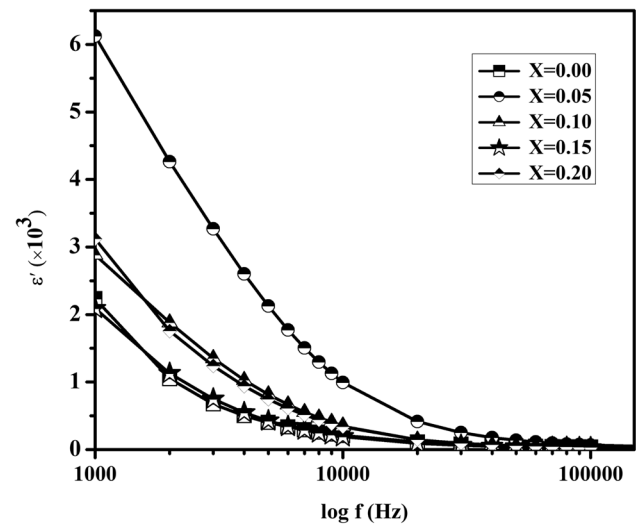
that the Q grew along with the frequency. The loss is a result of domain wall motion delaying the applied magnetic field that is alternating, and it is related to several domain phenomena, including non-repetitive and non-uniform domain wall motion, localized flux density variations, domain wall bowing, and domain wall nucleation and extinction [56].

4.10 Dielectric properties

The frequency dependence of dielectric constants are presented in Figs. 13 and 14 for mixed ferrites. These figures show the frequency-dependent variations of the dielectric constant for mixed Mn-Zn-V ferrites of various compositions. They show how the dielectric constant value declines steadily with increasing frequency. For $Mn_{0.5}Zn_{0.5}V_{0.05}Fe_{1.95}O_4$, the variation of the real and imaginary parts of the dielectric constant is at its highest. In these materials, the dielectric constant varying with frequency is described as a consequence of the effective value of polarization due to the inter-ionic, particle, and grain boundary effects at low frequencies. The lower dielectric constant values at high frequencies are imposed to a lower polarization contribution due exclusively to inter-ionic type. This explanation is made possible by the discharge of charge carriers from the high-frequency region's polarization effect. The response of polarization with frequency may be described using a principle laid down by Koops theory [57] i.e., the dielectric constant is the root mean square of the conductivity. Hopping of charge carriers (electrons) between $Fe^{2+} \leftrightarrow Fe^{3+}$ and $Mn^{2+} \leftrightarrow Mn^{3+}$ is the main mechanism of electrical conductivity [58, 59].

Fig. 14 The frequency dependence of ε″ of Vanadium Substituted $Mn_{0.5}Zn_{0.5}V_xFe_{2-x}O_4$, for (x=0, x=0.05, x=0.1, x=0.15, x=0.20)
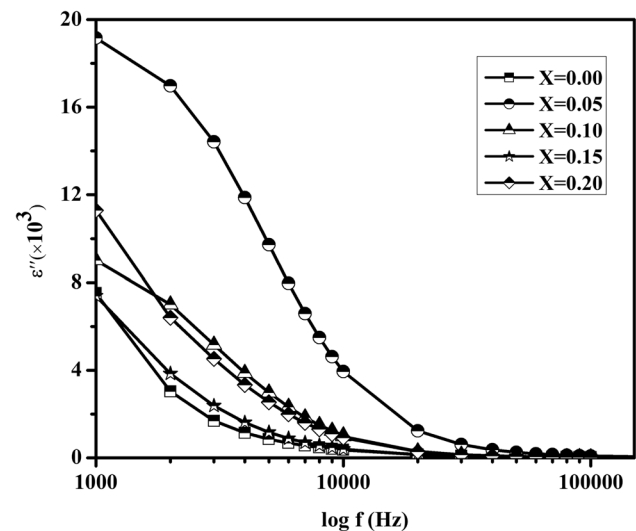
In Fig. 15 the frequency dependence of dielectric loss (tanδ) with respect to the frequency is shown. The dielectric loss increases to a maximum and then depicts a decreasing trend with increasing the frequency. The loss is highest when the supplied ac electric field's frequency is substantially lower than the frequency of electrons hopping between Fe^{2+} and Fe^{3+} ions at nearby octahedral sites. The loss is minimal at higher applied electric field frequencies because the electron exchange's hopping frequency is unable to keep up with the field's applied frequency past a certain critical frequency. Figure 15 provide a picture of the energy absorption carried by the electromagnetic field when it propagates through the ferrite. It is more at high frequencies as the number of charge carriers in this range is large.

4.11 Electrical properties

Frequency (f) dependence resistivity is an essential electrical characteristic as an inherent feature of magnetic materials since ferrites have a wide range of frequency dependence uses. The AC resistivity (ρ) of $Mn_{0.5}Zn_{0.5}V_xFe_{2-x}O_4$ sintered at 1250 °C was measured and plotted as a function of frequency (f) from 1 kHz to 1 MHz (Fig. 16). Figure 16 depicts the variation of AC resistivity with the frequency of undoped and V-replaced Mn–Zn ferrites. The V-replaced Mn–Zn ferrite has greater resistivity values at lower frequencies than the unmodified ferrite (for x = 0.15), indicating that the V-modified samples have poorer conductivity than the unmodified ones.

The published finding mentioned in ferrites frequently appears with tanδ variation research, in which samples with the lowest tanδ value have high resistivity and vice versa. Figure 16 shows that the AC resistivity drops fast as

Fig. 15 The frequency dependence of dielectric loss tangent of Vanadium Substituted $Mn_{0.5}Zn_{0.5}V_xFe_{2-x}O_4$, for (x=0, x=0.05, x=0.1, x=0.15, x=0.20)

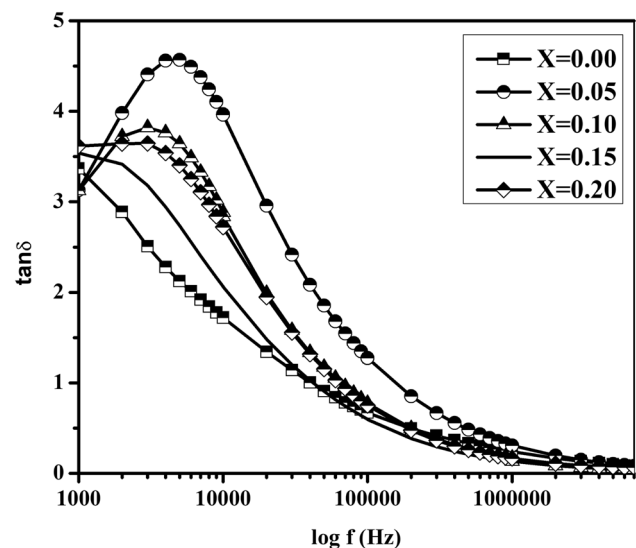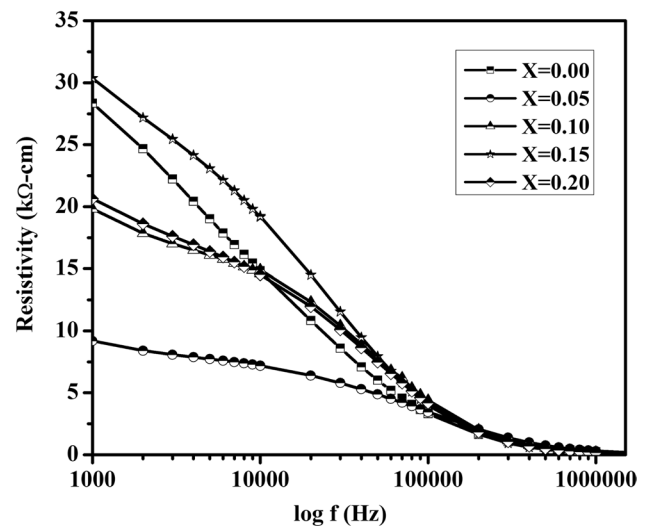**Fig. 16** Variation of A.C resistivity with frequency of Vanadium Substituted $Mn_{0.5}Zn_{0.5}V_xFe_{2-x}O_4$, for (x = 0, x = 0.05, x = 0.1, x = 0.15, x = 0.20)


the frequency rises from 1 kHz to 1 MHz, then drops slowly and constantly above 1 MHz for both undoped and doped Mn–Zn ferrites. Furthermore, an increase in the value of the resistivity of the Mn–Zn ferrite has been seen when the V content increases, which might be because of the partial substitution of Fe^{3+} ions by V^{3+} ions in the ferrite products. As a result, partial substitution of Fe^{3+} ions with V^{3+} ions decreases the number of iron ions existing for the conduction at the B-site, causing an increase in resistivity.

In the other hand, Fig. 17 shows a slow change in conductivity values in the beginning and an increase at the end of the frequency scale. The conductivity trend shows that V-doped ferrites have more electrons available for transport at high frequencies than undoped one.

5 Conclusions

The ceramic procedure was employed to produce $Mn_{0.5}Zn_{0.5}V_xFe_{2-x}O_4$ ferrites. The substitution of vanadium significantly affects the material's microstructure and electromagnetic characteristics. X-ray diffraction results confirmed the formation of single-phase spinel ferrites. With increasing vanadium content, the cell parameter declined marginally but insignificantly, and bulk density increased until x = 0.05 and subsequently decreased. Porosity increased in denser samples due to pores. The Rietveld refinement verified the samples' spinel structure and Fd-3 m space group. Because the substituent has a low melting point, the microstructural investigation demonstrated a rise in crystallite size and an increase in grain size. The Ms values have been dramatically reduced. The reduction in Y-K angles for this sample explains this. Magnetic permeability has reduced due to microstructural changes caused by the dopant. With an increase in loss, the dielectric

Fig. 17 The frequency dependence of A.C conductivity of Vanadium Substituted $Mn_{0.5}Zn_{0.5}V_xFe_{2-x}O_4$, for (x = 0, x = 0.05, x = 0.1, x = 0.15, x = 0.20)
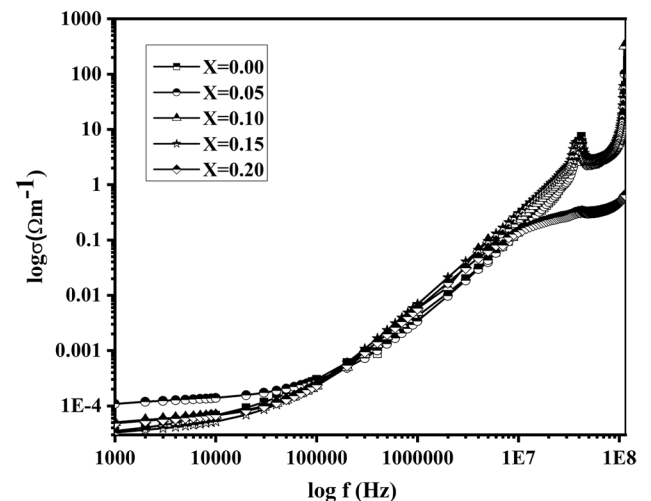
constant has been reduced. Low values of loss factor in the high-frequency region prove the compatibility of this V-doped ferrite to use in high-frequency applications. It's worth noting that vanadium doping improves resistivity, especially when x = 0.15. From this concentration forward, grains are the only source of resistance. With increasing vanadium content, long-distance charge carrier motions have a narrower frequency range. The increase in resistivity indicates that eddy current losses are reduced, suggesting that the material is a good choice for power applications.

Data availability The data generated this work are available from the corresponding authors upon reasonable request.

Code availability Not applicable.

Declarations

Competing interests The authors declare that they have no known competing financial interests or personal relationships that could have appeared to influence the work reported in this paper.

References

1. Raghuvanshi S, Mazaleyrat F, Kane SN. Mg1-xZnxFe2O4 nanoparticles: Interplay between cation distribution and magnetic properties. AIP Adv. 2018. https://doi.org/10.1063/14994015.
2. Batoo KM, Kumar S, Lee CG, Alimuddin. Influence of Al doping on electrical properties of Ni-Cd nano ferrites. Curr Appl Phys. 2022;9(4):826–32. https://doi.org/10.1016/j.cap.2008.08.001.
3. Ravinder D, Suresh K. Electrical conductivity of gadolinium substituted Mn-Zn ferrite. Mater Lett. 2000;44(3):253–5. https://doi.org/10.1016/S0167-577X(00)00038-0.
4. Hessien MM, Rashad MM, El-Barawy K, Ibrahim IA. Influence of manganese substitution and annealing temperature on the formation, microstructure and magnetic properties of Mn-Zn ferrites. J Magn Magn Mater. 2008;320(9):1615–21. https://doi.org/10.1016/j.jmmm.2008.01.025.
5. Zhang CF, Zhong XC, Yu HY, Liu ZW, Zeng DC. Effects of cobalt doping on the microstructure and magnetic properties of Mn-Zn ferrites prepared by the co-precipitation method. Phys B Condens Matter. 2009;404(16):2327–31. https://doi.org/10.1016/j.physb.2008.12.044.
6. Mathew DS, Juang RS. An overview of the structure and magnetism of spinel ferrite nanoparticles and their synthesis in microemulsions. Chem Eng J. 2007;129(1–3):51–65. https://doi.org/10.1016/j.cej.2006.11.001.
7. Somvanshi SB, Kharat PB, Khedkar MV, Jadhav KM. Hydrophobic to hydrophilic surface transformation of nano-scale zinc ferrite via oleic acid coating: magnetic hyperthermia study towards biomedical applications. Ceram Int. 2020;46(6):7642–53. https://doi.org/10.1016/j.ceramint.2019.11.265.
8. Patade SR, Andhare DD, Somvanshi SB, Jadhav SA, Khedkar MV, Jadhav KM. Self-heating evaluation of superparamagnetic MnFe2O4 nanoparticles for magnetic fluid hyperthermia application towards cancer treatment. Ceram Int. 2020;46(16):25576–83. https://doi.org/10.1016/j.ceramint.2020.07.029.
9. Kharat PB, Somvanshi SB, Somwanshi SB, Mopari AM. Synthesis, characterization and hyperthermic evaluation of PEGylated superparamagnetic MnFe2O4 ferrite nanoparticles for cancer therapeutics applications. Macromol Symp. 2021;400(1):2100130. https://doi.org/10.1002/masy.202100130.
10. Kalaiselvan CR, Laha SS, Somvanshi SB, Tabish TA, Thorat ND, Sahu NK. Manganese ferrite (MnFe2O4) nanostructures for cancer theranostics. Coord Chem Rev. 2022;473:214809. https://doi.org/10.1016/J.CCR.2022.214809.
11. Zapata A, Herrera G. Effect of zinc concentration on the microstructure and relaxation frequency of Mn-Zn ferrites synthesized by solid state reaction. Ceram Int. 2013;39(7):7853–60. https://doi.org/10.1016/j.ceramint.2013.03.046.
12. Latha K, Mohan KS, Ravinder D. Dielectric behaviour of mixed MnZn ferrites. Phys Status Solidi. 1994;142(2):K103–6. https://doi.org/10.1002/pssa.2211420240.

13. Sun L, et al. Effect of Zn2+ doping on the structural, magnetic and dielectric properties of MnFe2O4 prepared by the sol–gel method. J Mater Sci Mater Electron. 2018;29(7):5356–62. https://doi.org/10.1007/s10854-017-8501-2.

14. Schell J, et al. Thermal annealing effects in polycrystalline EuTiO3 and Eu2Ti2O7. AIP Adv. 2019. https://doi.org/10.1063/1.5115466.

15. Angadi VJ, et al. Structural, electrical and magnetic properties of Sc3+ doped Mn-Zn ferrite nanoparticles. J Magn Magn Mater. 2017;424:1–11. https://doi.org/10.1016/j.jmmm.2016.10.050.

16. Song J, Wang L, Xu N, Zhang Q. Microwave electromagnetic and absorbing properties of Dy3+ doped MnZn ferrites. J Rare Earths. 2010;28(3):451–5. https://doi.org/10.1016/S1002-0721(09)60132-0.

17. Heiba ZK, Mohamed MB, Ahmed SI. Cation distribution correlated with magnetic properties of cobalt ferrite nanoparticles defective by vanadium doping. J Magn Magn Mater. 2017;441:409–16. https://doi.org/10.1016/j.jmmm.2017.06.021.

18. Kaiser M. Magnetic and dielectric properties of low vanadium doped nickelzinccopper ferrites. J Phys Chem Solids. 2010;71(10):1451–7. https://doi.org/10.1016/j.jpcs.2010.07.011.

19. Maisnam M, Phanjoubam S, Sarma HNK, Prakash C, Devi LR, Thakur OP. Magnetic properties of vanadium-substituted lithium zinc titanium ferrite. Mater Lett. 2004;58(19):2412–4. https://doi.org/10.1016/j.matlet.2004.02.050.

20. S. State and L. Road. Dielectric properties of vanadium substituted. 2003; 17(21): 3881–3887.

21. Kaiser M. Influence of V2O5 ion addition on the conductivity and grain growth of Ni-Zn-Cu ferrites. Curr Appl Phys. 2010;10(4):975–84. https://doi.org/10.1016/j.cap.2009.12.042.

22. Janghorban K, Shokrollahi H. Influence of V2O5 addition on the grain growth and magnetic properties of Mn-Zn high permeability ferrites. J Magn Magn Mater. 2007;308(2):238–42. https://doi.org/10.1016/j.jmmm.2006.05.023.

23. Hossain A, Esha IN, Elius IB, Khan MNI, Maria KH. Interrelation between cationic distribution and electromagnetic properties of vanadium-substituted Mn–Zn ferrites. J Mater Sci Mater Electron. 2021;32(1):977–92. https://doi.org/10.1007/s10854-020-04874-7.

24. Vinnik DA, et al. Crystal growth, structural characteristics and electronic structure of Ba1-xPbxFe12O19 (x = 0.23–0.80) hexaferrites. J Alloys Compd. 2020;844:156036. https://doi.org/10.1016/j.jallcom.2020.156036.

25. Vinnik DA, et al. Electromagnetic properties of BaFe12O19: Ti at centimeter wavelengths. J Alloys Compd. 2018;755:177–83. https://doi.org/10.1016/j.jallcom.2018.04.315.

26. Atuchin VV, et al. Flux crystal growth and the electronic structure of BaFe12O19 hexaferrite. J Phys Chem C. 2016;120(9):5114–23. https://doi.org/10.1021/acs.jpcc.5b12243.

27. Praveena K, Sadhana K, Virk HS. Structural and magnetic properties of MN-ZN ferrites synthesized by microwave-hydrothermal process. Solid State Phenom. 2015;232:45–64. https://doi.org/10.4028/www.scientific.net/SSP.232.45.

28. Ewais EMM, Hessien MM, El-Geassy AHA. In-situ synthesis of magnetic Mn-Zn ferrite ceramic object by solid state reaction. J Aust Ceram Soc. 2008;44(1):57–62.

29. Rath C, et al. Dependence on cation distribution of particle size, lattice parameter, and magnetic properties in nanosize Mn-Zn ferrite. J Appl Phys. 2002;91(3):2211–5. https://doi.org/10.1063/1.1432474.

30. Solyman S. Transport properties of La-doped Mn-Zn ferrite. Ceram Int. 2006;32(7):755–60. https://doi.org/10.1016/j.ceramint.2005.05.018.

31. Hossain MD, et al. Tailoring the properties of Ni-Zn-Co ferrites by Gd3+ substitution. J Magn Magn Mater. 2020;497:165978. https://doi.org/10.1016/j.jmmm.2019.165978.

32. Ali MA, et al. Study of physical properties towards optimizing sintering temperature of Y-substituted Mg-Zn ferrites. Results Phys. 2019;14:102517. https://doi.org/10.1016/j.rinp.2019.102517.

33. Ghazanfar U, Siddiqi SA, Abbas G. Structural analysis of the Mn-Zn ferrites using XRD technique. Mater Sci Eng B Solid-State Mater Adv Technol. 2005;118(1–3):84–6. https://doi.org/10.1016/j.mseb.2004.12.018.

34. Keluskar SH, Tangsali RB, Naik GK, Budkuley JS. High permeability of low loss Mn-Zn ferrite obtained by sintering nanoparticle Mn-Zn ferrite. J Magn Magn Mater. 2006;305(2):296–303. https://doi.org/10.1016/j.jmmm.2006.01.018.

35. Abdel Maksoud MIA, El-Sayyad GS, Abokhadra A, Soliman LI, El-Bahnasawy HH, Ashour AH. Influence of Mg2+ substitution on structural, optical, magnetic, and antimicrobial properties of Mn–Zn ferrite nanoparticles. J Mater Sci Mater Electron. 2020;31(3):2598–616. https://doi.org/10.1007/s10854-019-02799-4.

36. Arulmurugan R, Jeyadevan B, Vaidyanathan G, Sendhilnathan S. Effect of zinc substitution on Co-Zn and Mn-Zn ferrite nanoparticles prepared by co-precipitation. J Magn Magn Mater. 2005;288:470–7. https://doi.org/10.1016/j.jmmm.2004.09.138.

37. Al-Mokdad F, Hassan RS, Awad R. Physical and dielectric properties of MnFe2O4 doped by Mo. Curr Nanomater. 2019;4(2):125–36. https://doi.org/10.2174/2405461504666190405153730.

38. Elius IB, et al. Synthesis and characterization of strontium doped barium titanates using neutron diffraction technique. Nucl Sci Appl. 2019;28(1):57–62.

39. C. A. Buckner et al. We are IntechOpen , the world ′s leading publisher of Open Access books Built by scientists , for scientists TOP 1 %," Intech, vol. 11, no. tourism, p. 13, 2016. https://www.intechopen.com/books/advanced-biometric-technologies/liveness-detection-in-biometrics.

40. Hossain A, Esha IN, Elius IB, Khan MNI, Maria KH. Interrelation between cationic distribution and electromagnetic properties of vanadium-substituted Mn–Zn ferrites. J Mater Sci Mater Electron. 2021;32(1):977–92. https://doi.org/10.1007/s10854-020-04874-7.

41. Lakshminarayana V, Chandramouli K, Rao GSN. Improved electromagnetic properties of vanadium doped Ni- Zn ferrite for high frequency applications. Int J Sci Res Phys Appl Sci. 2019;7(2):89–92. https://doi.org/10.26438/ijsrpas/v7i2.8992.

42. Sen SK, Paul TC, Dutta S, Hossain MN, Mia MNH. XRD peak profile and optical properties analysis of Ag-doped h-MoO3 nanorods synthesized via hydrothermal method. J Mater Sci Mater Electron. 2020;31(2):1768–86. https://doi.org/10.1007/s10854-019-02694-y.

43. Kayani ZN, Iram S, Rafi R, Riaz S, Naseem S. Effect of Cu doping on the structural, magnetic and optical properties of ZnO thin films. Appl Phys A Mater Sci Process. 2018;124(7):137–50. https://doi.org/10.1007/s00339-018-1886-9.

44. Nagamani K, Revathi N, Prathap P, Lingappa Y, Reddy KTR. Al-doped ZnS layers synthesized by solution growth method. Curr Appl Phys. 2012;12(2):380–4. https://doi.org/10.1016/j.cap.2011.07.031.

45. Rai R, Triloki T, Singh BK. X-ray diffraction line profile analysis of KBr thin films. Appl Phys A Mater Sci Process. 2016;122(8):1–11. https://doi.org/10.1007/s00339-016-0293-3.

46. Maria KH, Akther US, Esha IN, Hossain MS, Khan MNI. Estimation of structural, electrical, and magnetic variations of Mn-Ni- Zn ferrites by substituting rare earth Y3+ for high-frequency applications. J Supercond Nov Magn. 2020;33(7):2133–42. https://doi.org/10.1007/s10948-020-05471-9.

47. Jain GC, Das BK, Tripathi RB, Narayan R. INFLUENCE OF VsOs ON THE DENSIFICATION AND THE MAGNETIC PROPERTIES OF Ni-Zn FERRITE. J Magn Magn Mater. 1979;14:80–6.

48. Hartman P, Chan HK. Application of the periodic bond chain (PBC) theory and attachment energy consideration to derive the crystal morphology of hexamethylmelamine. Pharm Res An Off J Am Assoc Pharm Sci. 1993;10(7):1052–8. https://doi.org/10.1023/A:1018927109487.

49. Hakim MA, Nath SK, Sikder SS, Hanium Maria K. Cation distribution and electromagnetic properties of spinel type Ni-Cd ferrites. J Phys Chem Solids. 2013;74(9):1316–21. https://doi.org/10.1016/j.jpcs.2013.04.011.

50. Chithambararaj A, Bose AC. Hydrothermal synthesis of hexagonal and orthorhombic MoO3 nanoparticles. J Alloys Compd. 2011;509(31):8105–10. https://doi.org/10.1016/j.jallcom.2011.05.067.

51. Halder NC, Wagner CNJ. Separation of particle size and lattice strain in integral breadth measurements. Acta Crystallogr. 1966;20(2):312–3. https://doi.org/10.1107/s0365110x66000628.

52. Akhtar MN, et al. Evaluation of structural, morphological and magnetic properties of CuZnNi (CuxZn0.5−xNi0.5Fe2O4) nanocrystalline ferrites for core, switching and MLCI's applications. J Magn Magn Mater. 2017;421:260–8. https://doi.org/10.1016/j.jmmm.2016.08.035.

53. Arifuzzaman M, Hossen MB, Harun-Or-Rashid M, Rahman ML. Structural and magnetic properties of nanocrystalline Ni0.7-xCuxCd0.3Fe2O4 prepared through Sol-gel method. Mater Charact. 2021;171:110810. https://doi.org/10.1016/j.matchar.2020.110810.

54. Parvatheeswara Rao B, Kim CO, Kim CG. Influence of V2O5 additions on the permeability and power loss characteristics of Ni-Zn ferrites. Mater Lett. 2007;61(7):1601–4. https://doi.org/10.1016/j.matlet.2006.07.191.

55. A Anwar, A Akter, M N I Khan. Influence of Mn2+ substitution on structural, morphological, electrical, and magnetic properties of Ba04Ca04Sr0.2MnxTi1-xO3 perovskites. AIP Adv. 2020; 10(4): 11. https://doi.org/10.1063/5.0003294.

56. Overshott K. The causes of the anomalous loss in amorphous ribbon materials. IEEE Trans Magn. 1981;17(6):2698–700. https://doi.org/10.1109/TMAG.1981.1061648.

57. Chandrasekaran G, Selvanandan S, Manivannane K. Electrical and FTIR studies on Al substituted Mn-Zn mixed ferrites. J Mater Sci Mater Electron. 2004;15(1):15–8. https://doi.org/10.1023/A:1026276501072.

58. Jonker GH. Analysis of the of Cobalt. J Phys Chem Solids. 1959;9:165–75.

59. I. J. Pkys. Lithium antim ony ferrite. 1999; 182(2): 175–182.